
This is an electronic reprint of the original article.
This reprint may differ from the original in pagination and typographic detail.

Vodovozov, Valery; Aksjonov, Andrei; Petlenkov, Eduard; Raud, Zoja

Neural network-based model reference control of braking electric vehicles

Published in:
Energies

DOI:
[10.3390/en14092373](https://doi.org/10.3390/en14092373)

Published: 22/04/2021

Document Version
Publisher's PDF, also known as Version of record

Published under the following license:
CC BY

Please cite the original version:
Vodovozov, V., Aksjonov, A., Petlenkov, E., & Raud, Z. (2021). Neural network-based model reference control of braking electric vehicles. *Energies*, 14(9), Article 2373. <https://doi.org/10.3390/en14092373>

Article

Neural Network-Based Model Reference Control of Braking Electric Vehicles

Valery Vodovozov ^{1,*}, Andrei Aksjonov ², Eduard Petlenkov ¹ and Zoja Raud ¹

¹ Department of Electrical Engineering, Tallinn University of Technology, 19086 Tallinn, Estonia; eduard.petlenkov@ttu.ee (E.P.); learnelectronics@narod.ru (Z.R.)

² Electrical Engineering and Automation, Aalto University, FI-00076 Aalto, Finland; andrei.aksjonov@aalto.fi

* Correspondence: valery.vodovozov@gmail.com

Abstract: The problem of energy recovery in braking of an electric vehicle is solved here, which ensures high quality blended deceleration using electrical and friction brakes. A model reference controller is offered, capable to meet the conflicting requirements of intensive and gradual braking scenarios at changing road surfaces. In this study, the neural network controller provides torque gradient control without a tire model, resulting in the return of maximal energy to the hybrid energy storage during braking. The torque allocation algorithm determines how to share the driver's request between the friction and electrical brakes in such a way as to enable regeneration for all braking modes, except when the battery state of charge and voltage levels are saturated, and a solo friction brake has to be used. The simulation demonstrates the effectiveness of the proposed coupled two-layer neural network capable of capturing various dynamic behaviors that could not be included in the simplified physics-based model. A comparison of the simulation and experimental results demonstrates that the velocity, slip, and torque responses confirm the proper car performance, while the system successfully copes with the strong nonlinearity and instability of the vehicle dynamics.



Citation: Vodovozov, V.; Aksjonov, A.; Petlenkov, E.; Raud, Z. Neural Network-Based Model Reference Control of Braking Electric Vehicles. *Energies* **2021**, *14*, 2373. <https://doi.org/10.3390/en14092373>

Academic Editor:
Enrique Romero-Cadaval

Received: 17 March 2021
Accepted: 20 April 2021
Published: 22 April 2021

Publisher's Note: MDPI stays neutral with regard to jurisdictional claims in published maps and institutional affiliations.



Copyright: © 2021 by the authors. Licensee MDPI, Basel, Switzerland. This article is an open access article distributed under the terms and conditions of the Creative Commons Attribution (CC BY) license (<https://creativecommons.org/licenses/by/4.0/>).

1. Introduction

A common paradox of contemporary energy converters is that while their specific performance improves with each passing year, the overall conversion performance is getting worse. Transportation is one of the areas affected by this regression. The average efficiency of vehicle engines increases annually. However, rising car ownership, heavier vehicles, much more frequent trips, and longer distances travelled per capita have driven the sector's efficiency down from 26% to 21% over the past 70 years [1].

Since 20 to 70% of the vehicle energy is lost during deceleration [2,3], the problem of braking energy recovery is currently of great importance for improving the situation. A growth of competence in the management of braking road vehicles remarkably affects their energy efficiency [4]. Research in the field of both gradual braking modes and intensive antilock braking systems (ABS) have significantly been boosted in recent decades, filling up multiple books, reports, and research papers [5]. The first field relates to downhill driving, deceleration before traffic lights, parking, and similar regimes, where the driver reduces the velocity of the car in a stable and smooth manner. In this area, many interesting and useful electric vehicle (EV) energy saving solutions have been found [6,7]. In the second case, the driver tries to stop the vehicle abruptly, often without taking into account specific environmental conditions such as slippery surface, road slope, wind strength, cornering, etc. Very little research on energy saving under heavy braking can be found [8]. Even less attention is paid to energy recycling solutions that are so versatile that they could be equally successful in both braking scenarios [9].

The challenge lies in the contradiction between the specific energy needs that arise during an intensive stop and a stop with recuperation. Since the deceleration is commonly

great in the former case, the friction (hydraulic) brakes (FB) are used here, which convert the friction force into heat. In the latter case, the energy is directed to regenerative electrical braking (EB), restricted in terms of the state of charge (SOC), voltage, and current. To resolve this contradiction, blended braking systems are designed that combine traditional FB and EB, being associated with hybrid energy storage (HES) equipment composed of batteries on one side and ultracapacitors or/and flywheels on the other [10]. They help reclaim energy loss in braking, reduce car maintenance costs and tire particle emission, and extend driving range and time. These benefits are based on the main advantages of EVs in the sense of braking management, such as fast and accurate torque generation by electrical motors, easy torque measurement by current sensing, precise wheel speed encoding, and the ability to adjust each wheel independently due to the small motor dimensions [11]. However, in most existing braking control strategies, regenerative braking force is only a small fraction of the total braking effort, which contributes to safe braking but leads to poor braking economics [12].

With both the EB and FB, the braking strength is to be additionally limited to avoid skidding due to tire-road friction weakening. At present, there are no affordable sensors to identify nonlinear and nonstationary tire-road friction and make these data available to a braking controller [13]. Despite numerous attempts, an accurate and general mathematical model of tire behavior has not been obtained. Therefore, some indirect estimates are needed that look problematic in general and complicated by the fact that tire properties depend on variable road conditions and many other features.

In contrast to friction, wheel slip can be calculated easily as follows:

$$\lambda = \frac{v - \omega r}{v} \quad (1)$$

where v —longitudinal vehicle velocity, ω —angular wheel speed, and r —effective radius of the wheel. EVs usually utilize wheel-based sensors to measure the angular speed and/or angular acceleration of the wheel. In [14], the slip is derived based on velocity sensor signals and vehicle geometry. In [15], a perturbed sliding mode observer is used. A number of different techniques have been proposed as well to estimate EV velocity [16].

Several methods are available in the literature to transfer from the slip to friction; they include Pacejka's "Magic Formula", Burckhardt model, Rill model, and others [11,17,18]. Nevertheless, there exist diverse views on how to apply the obtained friction-slip estimates to ensure both the requested stopping rate and maximal energy recovery, taking into account that friction peak optimality for a given road surface is variable. In particular, in [9], the highest friction is developed at the slip level of about 12% on the dry road and at 5% on the icy road. On the contrary, in [16], the biggest friction appeared at 20% slip for dry road and 30% for icy road. Usually, the location of these peaks depends on the initial car velocity and alternates for forward-rear and right-left wheels. Hence, to avoid skidding, the designers commonly offer to choose some understated slip level, say 10% [16]. As a result, the vehicle does not decelerate fast enough and does not save as much energy as desired.

To exclude the above vagueness, in [9], the torque gradient control method is designed, where the derivative of the application torque T with respect to slip λ , $\frac{dT}{d\lambda}$, is used as a control feedback instead of the slip applied in conventional intelligent braking ABS, such as [16]. The main benefit of this method is that it does not require any tire model for implementation. Therefore, this approach is further elaborated in this paper.

Aside from the difficulty in estimating such a critical parameter as the friction factor, another challenge is to develop a model of the entire vehicle, whose equations of motion are highly nonlinear and many factors are often unknown. Commonly, models with 2, 4, and even more degrees of freedom (DOF) are used. The simplest of these is the quarter-car model [19], which has two DOFs. In the 4-DOF half-car model, the vehicle body is described by a displacement in the vertical direction, one rotation, and one DOF for each wheel vertical displacement. The 14-DOF model involves the longitudinal, lateral, and

vertical motions, pitch, roll, and yaw rotations, vertical motions of unsprung mass, and rotations of wheels [20]. The 38-DOF model [21] consists of 6 DOFs of vehicle and 8 DOFs for each wheel. In [22], the vertical and longitudinal vehicle dynamics are taken into account. In all models, the designer has to choose the appropriate level of fidelity, deciding whether or not to include many other effects, such as weight transfer across tires due to acceleration, lag in tire force generation with rapid steering movement, etc. [16,23].

After the development of the vehicle model, the controller is mastered based on data on the driving conditions and vehicle braking capabilities [17].

The main contender to control the gradual braking is a proportional-integral-differential controller (PIDC [24,25]). Classical PIDCs are easy to implement, and sufficient tuning rules are available to achieve a compromise in approaching rapid response and small overshoot [26], based on the famous Ziegler-Nichols and Refined Ziegler-Nichols formulas. Regrettably, when the vehicle performs differently in different operating modes, its parameters cannot be fixed and need to be modified systematically. It is not only a waste of time, but also difficult to implement [27]. The PIDC cannot yield a fine performance in highly order, nonlinear, multi-input, and multi-output environment [28]. As well, they are ineffective and often fail in ABS and braking processes with relatively long dead time. For this reason, for instance, the PIDC, designed in [25], cannot optimize energy recycling due to its orientation to a fixed driving medium. The same can be said about solutions offered in [29–32] that relate not only to the PIDC, but also to the sliding mode [33,34] and the feedback linearization controllers [35].

As distinct from the PIDC, intelligent control equipment has proven to be an emerging and effective solution. This applies to fuzzy logic controllers (FLC), model predictive, genetic algorithm, and neural network (NN) based controllers (NNC) capable to deal successfully with nonlinear, uncertain, and varying braking dynamics. Because of this, the scope of application of intelligent vehicles with highly nonlinear dynamics, driven upon the changeable road pavements, is growing annually [10,16].

The FLCs refer to rule-based controllers. The rule-based approach is considered as a conventional way of energy management; therefore, it is widely used by many vehicle manufacturers, such as Honda® and Toyota® [13,36]. Control here is defined based on a set of “if-then” rules that depend on human expertise, operation boundaries, and safety considerations. The advantages of these systems are their ease of computation and the simplicity in applying updates to commercially produced vehicles. A major drawback of the FLCs is that their quality is completely dependent on the professional level of a specialist who sets them up.

The NNCs can outperform human experts used in FLC, and may be realized more accurately and quickly [27]. The target for using the NNCs is to capture the accuracy of experimental data while saving computational time, so that NN systems are usually designed within reasonable timeframes. This is why different NN methodologies are applied in braking systems of automobiles [35] and aircraft [37].

The study [38] is devoted to the use of various NNs in changing driving scenarios, demonstrating the effectiveness of the NNC in extensive and smooth testing modes. In [39], a robust NNC guarantees stability against unknown uncertainties. Emergency braking on a variable-surface road is considered here by tracking the reference wheel slip in different maneuvers. Another paper [16] contributes to the development of an effective engineering solution aimed at improving control of ABS by estimating the friction coefficient with the help of video data. An emerging deep learning method is applied in [22] for the classification of six road surface types and condition combinations: wet gravel, dry gravel, wet cobblestone, dry cobblestone, wet asphalt, and dry asphalt. An experimental investigation of the designed convolutional NN was carried out here to parametrize the vehicle tire model. In [40], a recurrent NN has been proposed as a drive cycle recognizer and NNC coefficient tuner. This network tracks the last 200 s of computed speed data (average, maximum, minimum speed, and acceleration), which are characteristic values for a drive

cycle. The NN has 6 input neurons, 10 neurons with a sigmoid function in the hidden layer, and a single-neural output layer.

The paper [41] represents an interesting example of an intelligent blended braking system. The NN control problem is formulated there as the search for optimal policy in the Markov decision-making process, where the braking space is defined as a set of actions that include no braking, weak braking, average braking, and strong braking. The policy used to manage braking is implemented through computer simulation using deep reinforcement learning. Another intelligent braking system proposed in [12] considers two kinds of braking operations, namely, releasing of the accelerator pedal, and pressing the brake pedal. The radial basis function NN model is trained here through the optimal braking force, while the multiple correlation coefficient method is applied to analyze model errors against a sample database. Several standard test cycles, such as US06, UDDS, LA92, and ECE were used to test the system.

The NNCs are applied successfully in HES management to optimize energy recovery. For instance, a convolutional NN has been used in [42] for estimation of energy/power consumption of EV. In [43], a regenerative EB scheme is offered aiming to transfers braking energy to the HES devices. To this end, the multilayer feedforward NN provides satisfactory capability, comprising EV speed and SOC of the supercapacitor and battery banks in a number of braking situations. As well, [44] uses real data collected over two days of power consumption, trip time, and SOC as training inputs to the NN. The NN output specifies the EV recommended operation mode as a function of time, whereas typical peak loads and off-peak load times, human behavior, seasonal and weather conditions contribute to the model to generate a realistic pattern. Another example is the deep NN-based approach of EV energy demand estimation proposed in [23]. It is based on the time series of the driving cycle properly preprocessed and transformed into 1D or 2D maps to serve as a static input to the NN. Several deep feedforward NN architectures are considered for this application along with various input formats. In [45], the HES-based braking system implements automatic control of the EV regeneration torque of the motor to improve driver's comfort and energy efficiency. To apply this system, an accurate prediction of the vehicle deceleration states was produced. The original EV deceleration model proposed in this paper is based on the deep NN consisting of a sequential recurrent NN with long-short-term memory and a two-layer conventional NN model.

One of the directions in implementation of the NNC into the on-board EV HES is focusing on determining the optimal coefficients of the classical PIDCs and their influence on the power distribution [46,47]. In [48], the NNC provides twice less transition time compared to the classical PIDC, along with a reduction of energy loss and motor overshoot. The proposed control method made it possible to automatically tune the PIDC, thus reducing the inrush currents and torque surges, and thereby prolonging the service life of vehicle mechanical components. In [49], an NNC replaces the PIDC to control the angular position of the wheel. This double-input NNC provides supervised learning, at which the dataset for training the NN is run before the simulation to get the output results. In [50], the PIDC with an NN uses three special types of neurons: P-neuron, I-neuron, and D-neuron that realize the three fundamental controlling actions. In [51], an adaptive NN-based PIDC is offered for the multi-input multi-output nonlinear vehicle system. Different combinations of NNC and FLC are proposed in [52] to control the EVs in blended braking. A neuro-fuzzy controller applied in [53] solves the torque distribution problem for regenerative braking of a hybrid bus. By merging the FLC and the backpropagation NNC, an algorithm for processing the bus velocity, wheel speed, and the brake pedal travel is implemented.

A successful combination of the NNC, sliding-mode controller, and PIDC is proposed in [54]. To reflect the nonlinear time-varying characteristics of the longitudinal dynamics, the NNC is designed based on a sliding mode controller and a single-neuron PIDC, which provides deceleration in emergency braking conditions. Co-simulation utilizing CarSim® and Simulink® was carried out on an intelligent vehicle model. Here, the sum of wind and rolling resistances was taken into account.

An objective of the current research is to offer a new NN-based control system, which ensures high quality blended braking of EVs in both intensive (ABS-fed) and gradual braking scenarios with energy recovery, taking into account the changing road pavement. The main contribution of the paper is in the design of the NNC capable to meet the conflicting requirements of different braking modes and road surfaces. This is the first study where the NN provides the torque gradient control without a tire model resulting in the return of maximal energy to the vehicle HES during the braking process.

Using the author's torque allocation algorithm, the system determines how to distribute a single driver's torque request into separate requests between the FB and EB. Multiple simulations demonstrate effectiveness of the proposed NN-based braking system. The model states and inputs are employed here as a guide for developing a coupled two-layer NN. Furthermore, a simulation study demonstrates that the designed system can cover various dynamic behaviors that could not be included in a simplified physics-based model. An experimental part of the research proves the validity of the model and simulations.

In the next sections, an NN-based braking system and its parts are introduced. Then, two design phases of the NNC are explained, namely, identifying the NN model, which predicts the EV behavior, and training the NNC using the identified NN model. Once the control system is trained and validated, its responses are estimated against the various driver's requests and environment conditions. To verify the effect of the proposed control strategy in the hardware environment, a set of experimentations is described. Finally, the results are discussed and conclusions are drawn.

2. Materials and Methods

2.1. Braking System

The braking system discussed in this paper (Figure 1) involves an NN-based Model Reference Controller (MRC), a torque allocator (TA) coupled to the physics-based model of an electric vehicle with blended braking (PBEV) supplied from a hybrid energy storage (HES), a reference system (REF), and computational modules that estimate wheel slip and torque gradient.

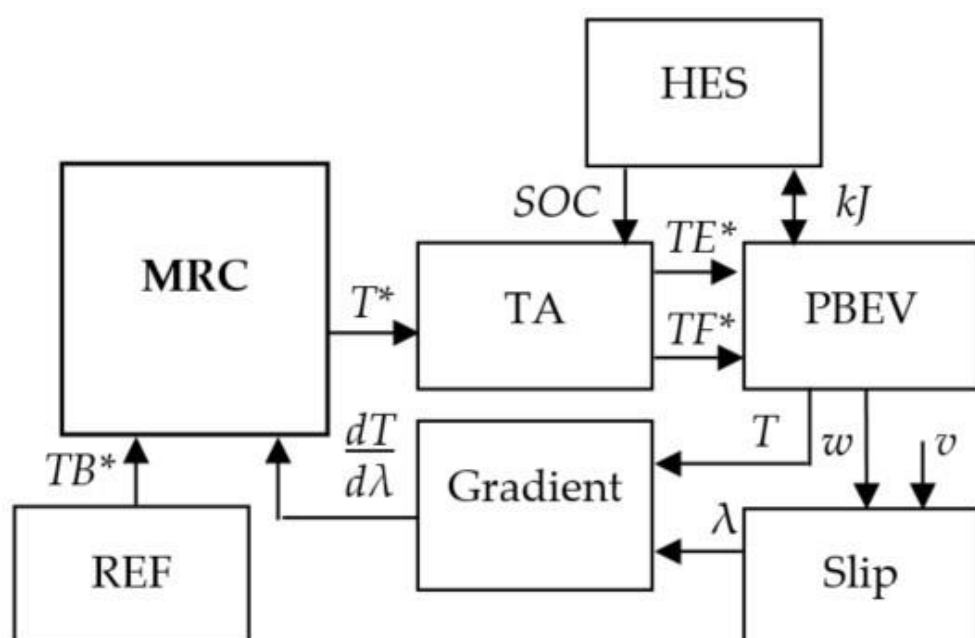


Figure 1. The architecture of the EV braking system.

The REF block simulates a driver pressing or releasing the brake pedal with different forces. The MRC block simulates the driver's pressing or releasing the brake pedal with different forces. The MRC unit produces the actuating torque T^* , further divided by the TA module into two fractions: electrical TE^* and friction TF^* , both entering the PBEV block. During braking, the HES block consumes the electrical fraction of the energy kJ generated by the PBEV, while its value does not exceed the permissible SOC, voltage, and current limits.

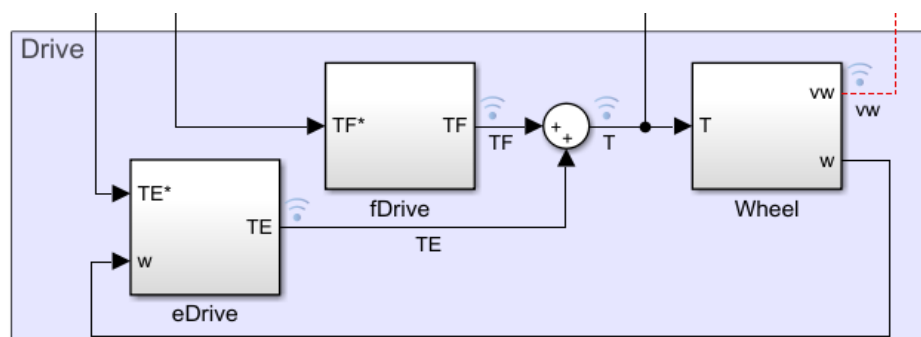
Figure 1. The architecture of the EV braking system.

The REF block simulates a driver pressing or releasing the brake pedal with desired forces. The MRC unit produces the actuating torque T^* , further divided by the TA into two fractions: electrical TE^* and friction TF^* , both entering the PBEV²² block. During braking, the HES block consumes the electrical fraction of the energy kJ generated by PBEV, while its value does not exceed the permissible SOC, voltage, and current restrictions. The application torque T of the PBEV decelerates the EV at such an intensity as to meet the driver's reference T_{BR} , on the one hand, and avoid wheel skidding caused by the wheel slip, on the other. The electrical current recharges the HES block from the EB, while the pressure signal adjusts the FB. Braking will complete when the driver releases the pedal or the vehicle stops.

2.2. Physics-Based Vehicle Model

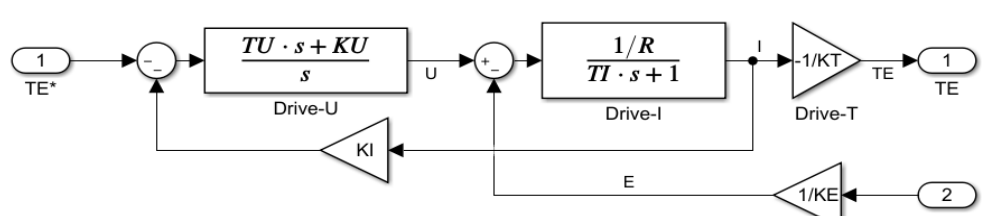
2.2. Physics-Based Vehicle Model

The physics-based vehicle model (PBEV) used in this study was initially established in [9] based on experimental data describing the interacted rotational properties and physical features of the EV. In Figure 2, its Simulink® composition is shown. It is made up of an adjustable electrical drive (eDrive) implementing a regenerative EB, a friction drive (fDrive) integrated with the EB and modelled as an inertial first-order chain with time, and a Wheel unit, which simulates the gear and vehicle inertia.

**Figure 2.** The physics-based Simulink® model of the vehicle.**Figure 2.** The physics-based Simulink® model of the vehicle.

To ensure direct torque control with consideration of the system non-linearity and space vector modulation, the AC6 Interior PM Synchronous Motor Drive block from the Specialized Power Systems MATLAB/Simulink® library is used as the EB core. It is composed of the following four main parts: the electrical motor of 288 V, 100 kW a three-phase voltage source inverter powered by a direct voltage from the IBS and composed of the following four main parts: the elliptical phasor of 288 V, 100 kW, angular speed ω , speed controller operating in the regulation mode, torque T , speed, power, current, and angle signals are available at the output of the blocks. The simulation of the system is discretized within 20 steps per second, which is applied for the space vector modulation in the interior PM synchronous motor device.

To facilitate the NN learning procedures, this block was represented by the replacement circuit shown in Figure 3.

**Figure 3.** The replacement circuit of the electrical drive used for NN learning.

Here, the Drive-U sub-block is responsible for direct torque control, electrical power supply, and energy recovery. Together with the Drive-I sub-block, it arranges a torque supply and energy recovery. Together with the Drive-I sub-block, it arranges a torque stabilization loop with a PI current regulator. The Drive-T sub-block and the Wheel block belong to the speed loop activated in gradual deceleration and shorted in emergency braking. In the Wheel block (Figure 4), the static fraction of the application torque (Static T) is taken into account when the velocity drops to a low vehicle settling velocity level (v_{home}) and the EB becomes ineffective.

Figure 3. The replacement circuit of the electrical drive used for NN learning.

Here, the Drive-U sub-block is responsible for direct torque control, electrical supply, and energy recovery. Together with the Drive-I sub-block, it arranges a stabilization loop with a PI current regulator. The Drive-T sub-block and the Wheel belong to the speed loop activated in gradual deceleration and shorted in emergency braking. In the Wheel block (Figure 4), gradual deceleration and shorted in emergency braking. In the Wheel block (Figure 4), the static fraction of the application torque (Static T) is taken into account when the velocity drops to a low vehicle settling velocity level (v_{home}) and the EB becomes ineffective.

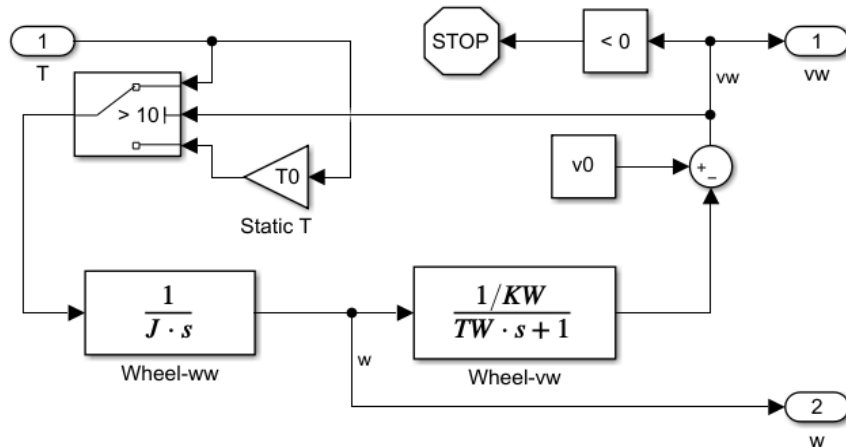


Figure 4. The Wheel block of the PBEV.

The data used in the simulation are presented in Table 1.

The data used in the simulation are presented in Table 1.

Table 1. The data used in the PBEV simulation.

Table 1. The data used in the PBEV simulation.

Symbol	Parameter	Unit	Value
K_E	Moment of inertia	kgm^2	10
J_KF	Electromotive force factor	Vs/rad	5
K_E^{KI}	Moment of inertia	kgm^2	1
K_E^{KT}	Current sensor factor	Nm/A	10
K_E^{KU}	Magnetomotive force factor	A/Nm	1
K_E^{KW}	Current loop gain	Vs/Nm	500
K_E^R	Gear ratio	rad/m	1
$K_T T_0$	Resistance of motor winding	Ohm	10^{-10}
$K_T T_0$	Saturation torque	Nm	10^{-10}
K_U^{TB}	Magnetomotive force factor	A/Nm	1
$K_U^{TB} *$	Actuating torque	Nm	10^{-10}
K_U^{TF}	Current loop gain	Vs/Nm	50
K_W^{TI}	Time constant of friction drive	s	0.1
K_W^{TI}	Time constant of current sensor	s	0.01
R_{TU}	Gear ratio	rad/m	1
T_s	Resistance of HES	Ohm	10^{-6}
v_{home}	Sampling time	s	2×10^{-6}
v_0	Vehicle settling velocity	m/s	10
v_0	Initial vehicle velocity	m/s	100

2.3. Torque Allocation

The torque allocation module TA algorithmically distributes the actuating braking torque T^* , generated at the MRC output, between the front and rear wheels in a fixed ratio [55] and allocates it between the FB and EB based on the real-time SOC, voltage, and permissible EB current.

To transfer the maximal fraction of the actuating torque T^* to the EB, the ability of the electrical drive to develop sufficient power, voltage, and current to charge all energy storage devices of the HES is used. Meanwhile, in order to keep the battery and the ultracapacitor within their proper SOC borders, the torque allocation algorithm verifies whether the electrical current and motor torque meet the real-time HES restrictions.

In [9], an appropriate torque allocation algorithm was offered. There, when the control system recognizes the actuating torque request T^* , the EB is activated, and either the ultracapacitor or the battery HES section runs. The FB torque does not appear until either

any of the SOC levels exceeds the allowed overcharging barriers or the electrical motor produces maximal power. As soon as the motor torque becomes insufficient, the system runs FB and EB together:

$$TF^* = T^* - TE^* \quad (2)$$

Only when both SOC levels exceed their boundaries, the solo FB is used due to the inability to regenerate. Therefore, a common trait of this strategy is to include regeneration in all braking scenarios, even during heavy braking with ABS, leaving the solo FB only if the HES is saturated.

2.4. Model Reference Controller

Using the data generated by the designed PBEV model, the NN-based MRC solves the problem of effective EV braking with maximal recovery of braking energy.

To design the NN, the Deep Learning Toolbox™ blockset from MATLAB/Simulink® was used in this study. An interactive development environment for the NN controllers was applied, namely the MRC block. In response to the reference in the form of the driver's torque request TB^* , the MRC issues an actuating braking torque command T^* to stop the PBEV without wheels locking under a variety of road conditions and EV velocities. The MRC includes two NNs, which are an NN controller (NNC) generating the actuating braking torque command and an NN model of the PBEV (NNEV) predicting its behavior.

Two stages of the MRC design were conducted (Figure 5), namely: (a) identification of the NNEV and (b) training the NNC using the identified NNEV. The aim of the NNEV identification was to obtain the NNEV parameters capable of representing the behavior of the unknown PBEV. The mean squared error (MSE) between the PBEV and NNEV outputs was used as the NNEV training signal (○).

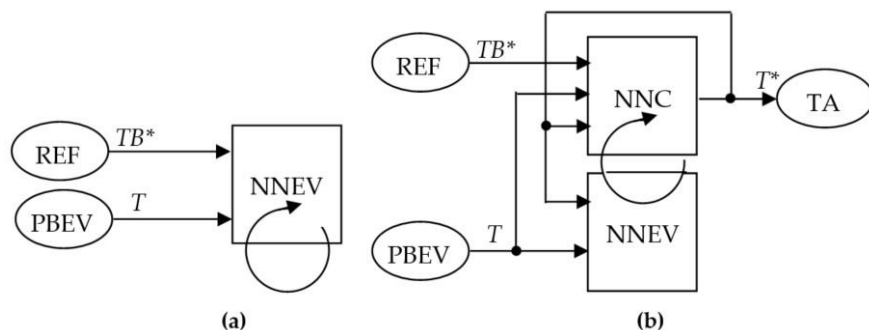


Figure 5. Two phases of the MRC design: (a) identification of the NNEV and (b) training the NNC.

In the NNEV, the feedforward topology is used and the NNC the recurrent one. In both NNs, double layer architecture is applied with delay lines that hold the previous values of braking torque in such a way that the input signals enter the input layers of the NNs in the next cycle. The MRC architecture characteristics are collected in Table 2.

Table 2. MRC architecture characteristics.

Architecture Parameter	Value	Value
Number of delayed NNEV inputs	2	2
Number of delayed NNEV outputs	2	2
Number of delayed NNC reference inputs	2	2
Number of delayed NNC feedback inputs	2	2
Number of delayed NNC outputs	1	2
Number of delayed NNC outputs		1

The REF block was adopted as a source to generate identification and training data. A variant of the Levenberg–Marquardt gradient descent algorithm [56] was employed for identification and training. Preliminarily, the samples were prepared that cover the range of expected MRC inputs. To prepare the training data, the reference training function *trainlm* was utilized consisted of a series of steps of random heights and random intervals. The main training sample characteristics are presented in Table 3.

range of expected MRC inputs. To prepare the training data, the reference training function *trainlm* was utilized consisted of a series of steps of random heights and random intervals. The main training sample characteristics are presented in Table 3.

Table 3. MRC training sample characteristics.

Sample Parameter	Unit	Value
Sampling interval	s	0.05
Number of samples		400
Maximum sample interval	s	2
Minimum sample interval	s	0.1
Maximum reference value		1
Minimum reference value		0

Since the MRC output is limited to 0 and 1, the sample datasets have been exposed to preprocessing. Both NNs were trained for function approximation (nonlinear regression) so that the MRC output follows the reference as closely as possible.

3. Results and Discussion

3.1. NNEV Identification

In the NNEV identification phase, the batch mode was enforced, in which 400 training samples given in Figure 6a (sections Network Architecture and Training Data) were applied to the NNEV before the weight updating. It was performed offline based on the measurements of the NNEV inputs and outputs of the system. The NNEV output (Figure 6b, Plant Input) was compared to the PBEV output (Figure 6b, Plant Output) aiming to minimize the MSE between the responses. To perform identification, the training data were shared among the training, validation, and testing phases as shown in Figure 6a (section Training Parameters). The number of training epochs was specified as 10 in this section. As follows from Figure 6b, the PBEV accurately follows the NNEV.

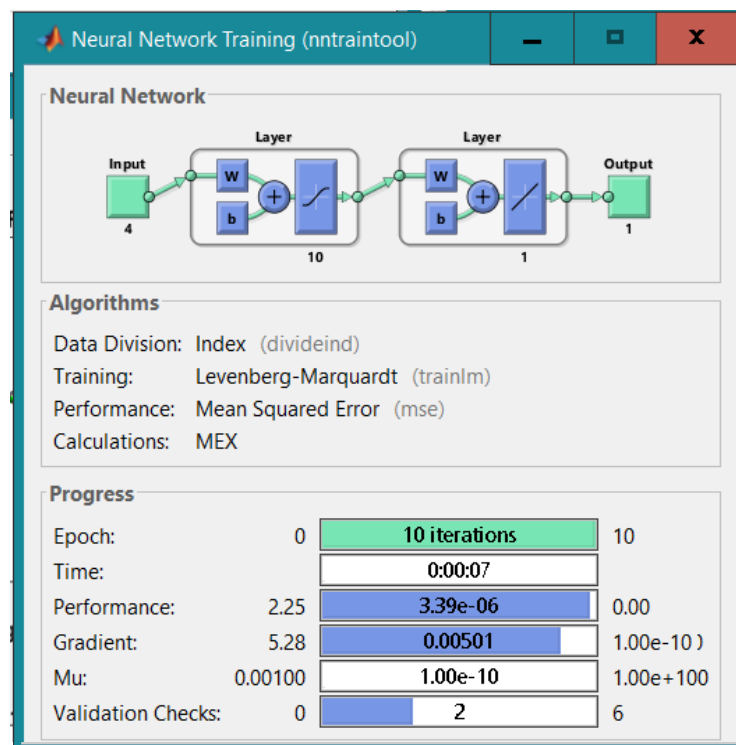
After performing identification, a final NNEV architecture was chosen, as shown in Figure 6c. It has 2 neurons in the input layer, 10 neurons in the only hidden layer with the sigmoid activation functions, and an output layer with a single neural linear activation function. The sigmoid *tansig* activation functions allow the NNEV to learn nonlinear relationships between inputs and output. The linear *purelin* activation function is suitable for solving the nonlinear regression problem related to the braking torque estimation. It was found that adding more hidden layers or hidden neurons does not improve the performance while increasing computation complexity, which is not desirable in a time critical context. Another obstacle to increasing the number of hidden layers might be the opacity of the system, which prevents effective security checks.

The NNEV identification results are shown in Figure 6c–e. The convergence curve of the model shows that MSE has almost converged at the 10th epoch where its value is of 7.6574×10^{-6} . Therefore, the model can be qualified as a well-trained one, and 10 epochs chosen for training are sufficient to meet the demands of the model application. The final regression of 0.99997 after training, validation, and testing also qualifies the model as a good one.

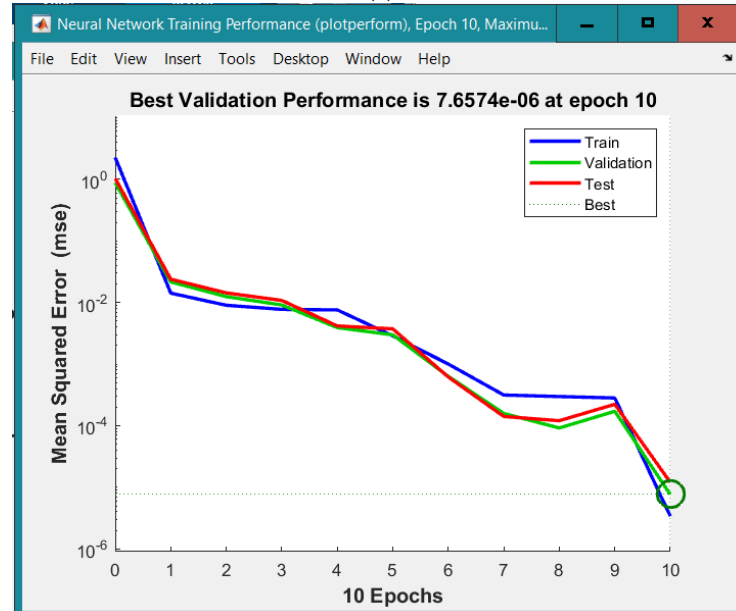
minimize the MSE between the responses. To perform identification, the training data were shared among the training, validation, and testing phases as shown in Figure 6a (section Training Parameters). The number of training epochs was specified as 10 in this section. As follows from Figure 6b, the PBEV accurately follows the NNEV.



Figure 6. Cont.

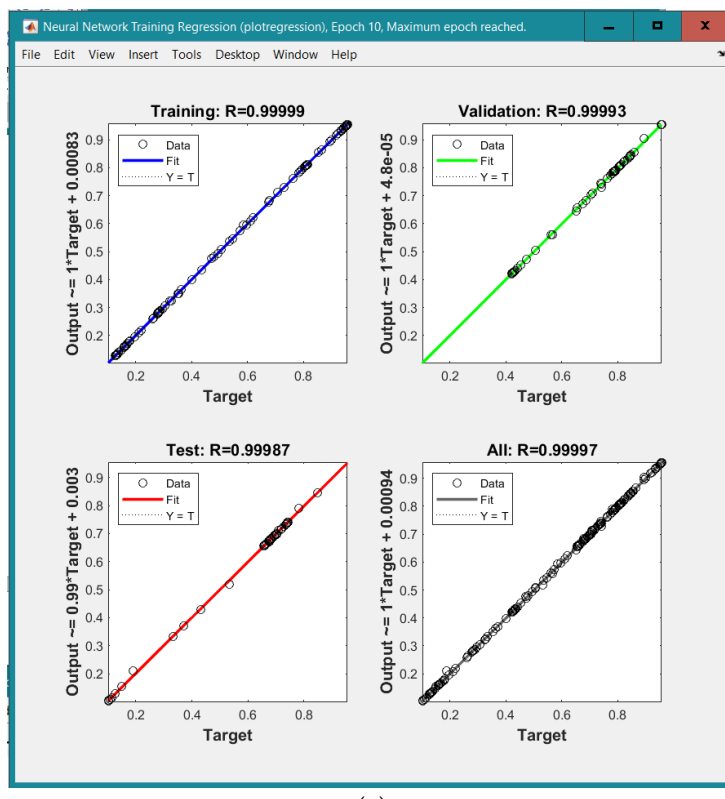


(c)



(d)

Figure 6. Cont.



(e)

Figure 6. NNEV identification: (a) conditions; (b) training data; (c) training result; (d) performance; (e) regression.

After performing identification, a final NNEV architecture was chosen, as shown in [Figure 6e](#). Among the activation functions used to train the NNC, the sigmoid function was chosen due to its fast convergence rate and its ability to perform computations backward through the NN. The NNC was trained using the PBEV model, having one input and one output to generate data for the MRC training algorithm. The strategy of training supports both the offline and online tuning of the NNC weights in a way that the MSE between the reference and the NNC output converges to zero.

The reference data displayed in Figure 7a,b are the same as for the NNEV identification. An NNC with three hidden layers was chosen to show how the number of hidden layers affects the performance of the NNC. The first layer has 10 neurons, the second has 5, and the third has 2. The total number of neurons in the NNC is 17. The NNC was trained using the PBEV model, having one input and one output to generate data for the MRC training algorithm. The strategy of training supports both the offline and online tuning of the NNC weights in a way that the MSE between the reference and the NNC output converges to zero. The reference data displayed in Figure 7a,b are the same as for the NNEV identification. An NNC with three hidden layers was chosen to show how the number of hidden layers affects the performance of the NNC. The first layer has 10 neurons, the second has 5, and the third has 2. The total number of neurons in the NNC is 17. The NNC was trained using the PBEV model, having one input and one output to generate data for the MRC training algorithm. The strategy of training supports both the offline and online tuning of the NNC weights in a way that the MSE between the reference and the NNC output converges to zero.

3.2. NNC Training and Validation

Once the NNEV is identified, it was used to train the NNC. Among the algorithms suitable for the NNC performance optimizing, the fastest of the gradient types was applied, namely, the backpropagation algorithm able to perform computations backward through the NN. The NNC was trained using the PBEV model, having one input and one output to generate data for the MRC training algorithm. The strategy of training supports both the offline and online tuning the NNC weights in a way that the MSE between the reference and the NNC output converges to zero.

The reference data displayed in Figure 7a,b are the same as for the NNEV identification. An NNC architecture was chosen, as shown in Figure 6c. It has one neuron in the input layer, four neurons in the hidden layer with the sigmoid activation functions, and

Energies 2021, 14, 2373

an output layer with a single neural linear activation function. To perform training, the reference data were broken into two segments. The number of training epochs for each segment was specified as 10.

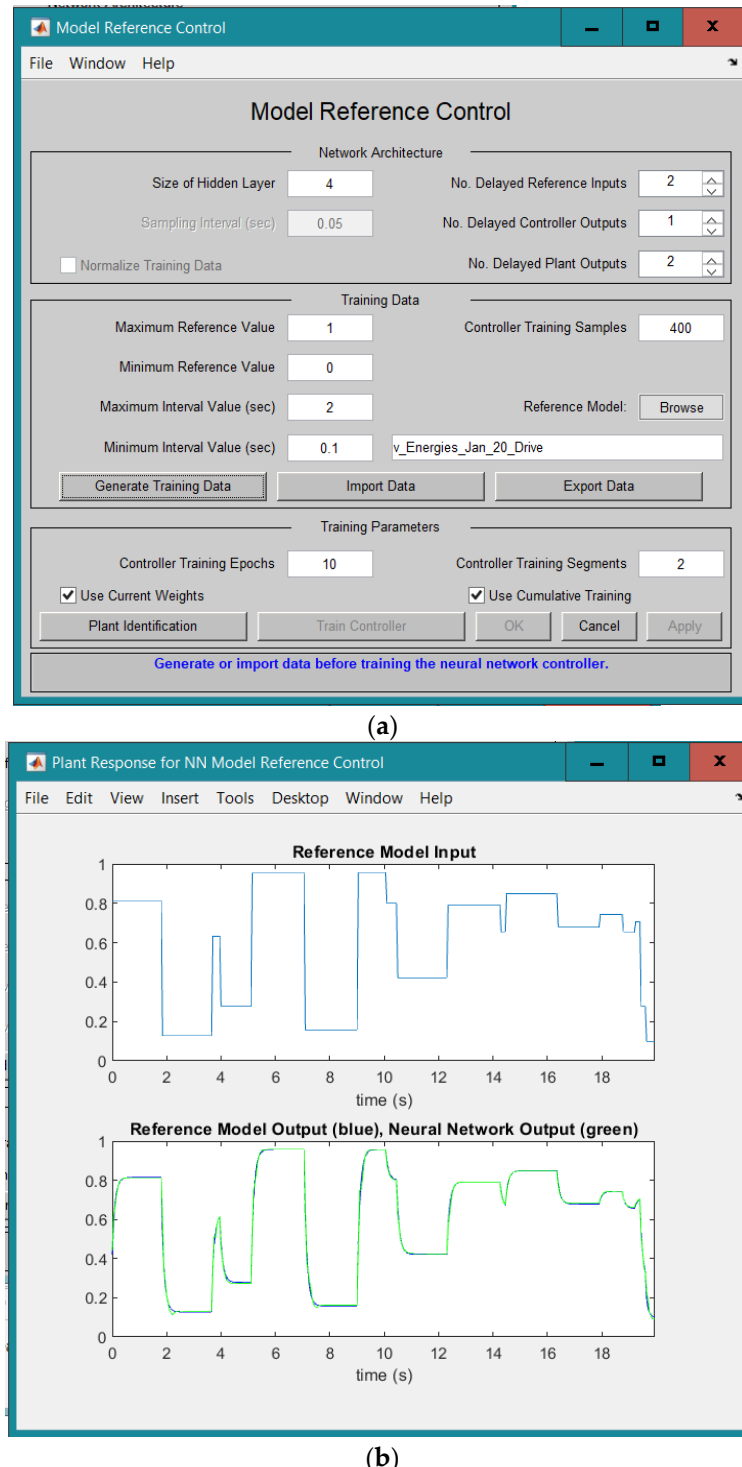
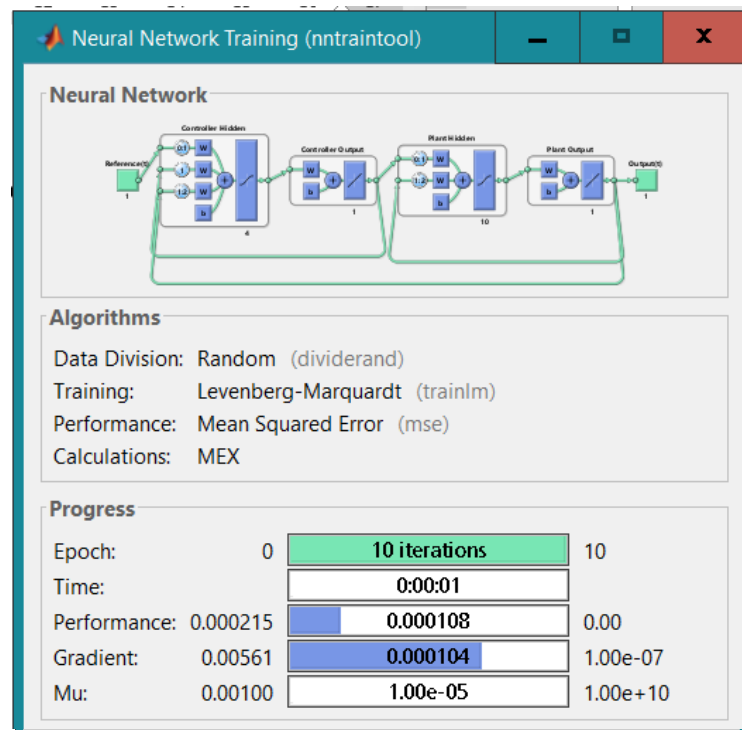
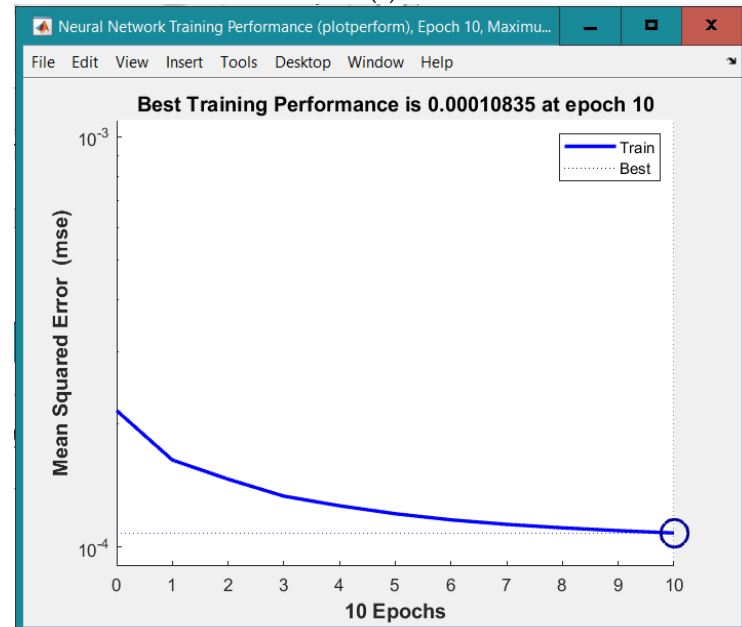


Figure 7. Cont.



(c)



(d)

Figure 7. Cont.

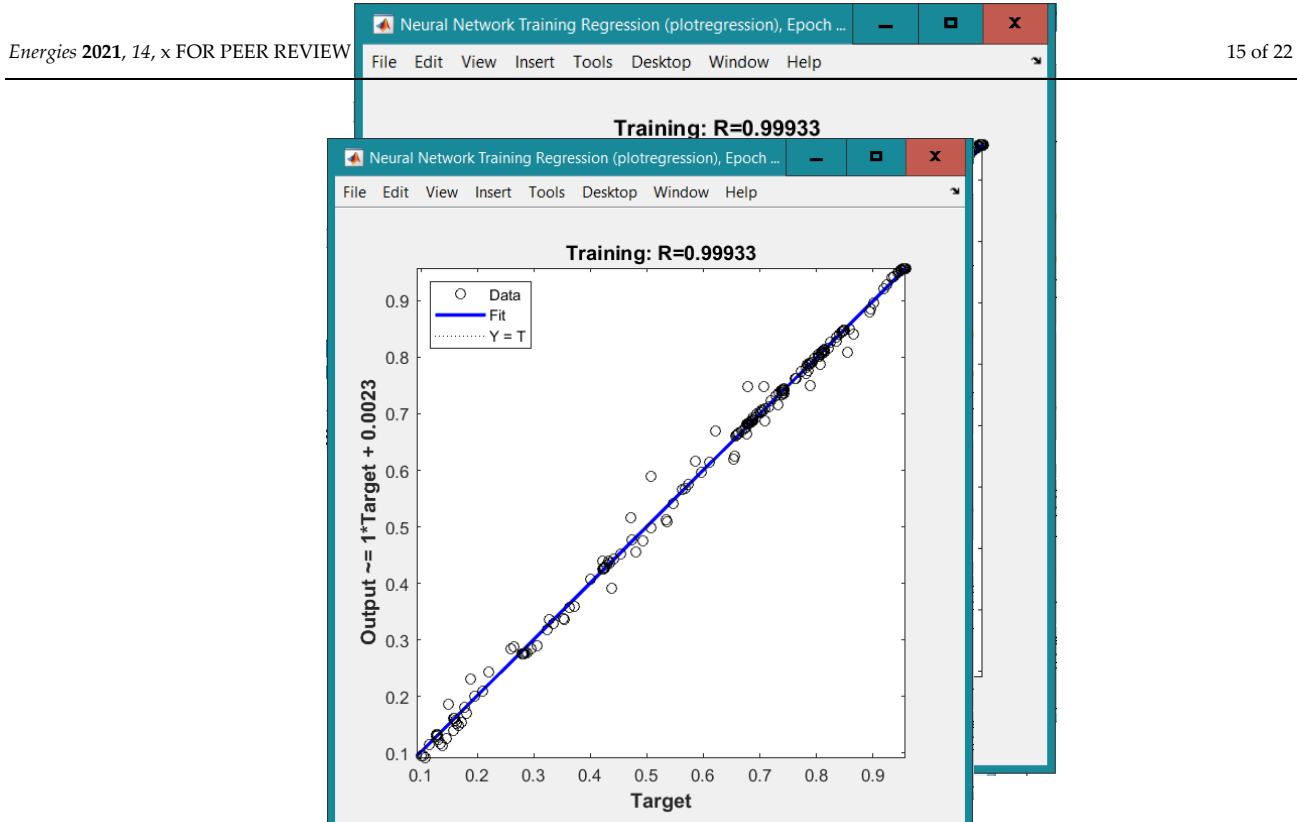


Figure 7. NNC training: (a) correlations; (b) training data; (c) training results; (d) performance; (e) regression.

The NNC training results are shown in Figure 7(e). As follows from these results, the NNC training of the MRC is very fast. Therefore, the optimization results obtained quickly after the first 10 epochs of the NNC convergence curve is the best. The convergence speed of the NNC is very fast, therefore, the optimization is obtained quickly. According to this convergence curve, the MSE has almost converged at the 10th epoch where its value is 108.35×10^{-6} . The regression of 0.99933 qualifies the NNC as well trained. The training of the MRC was validated using the double-step reference command (TB^*). After the training, the MRC was validated using the double-step reference command (TB^*) limiting the driver's brake pedal pressing/releasing. According to Figure 8, the response (T) of PBEV model to the MRC command (T^*) follows the driver's reference quite accurately; the maximal dynamics error is 100 Nm (10%) and the steady-state error is 9 Nm (1%).

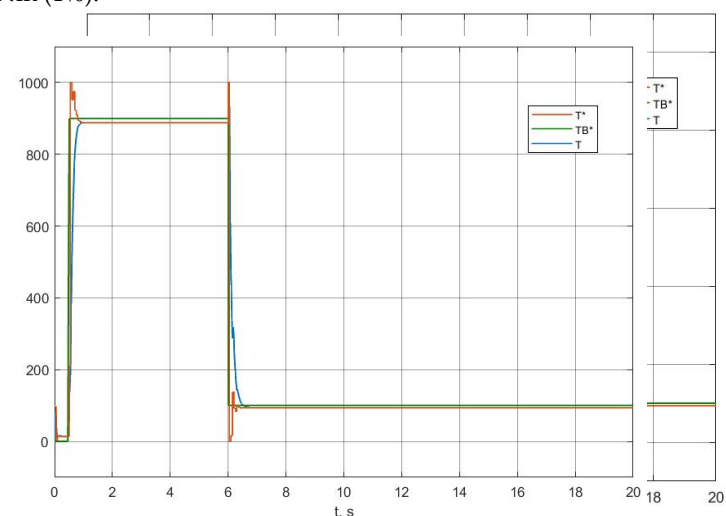


Figure 8. The responses of the MRC (T^*) and PBEV (T) to the double-step driver's reference (TB^*).

3.3. Experimental Data Used for the MRC Testing

After the MRC training and validation, the PBEV model responses were estimated against various driver requests and MRC commands. To test the effectiveness of the designed control strategy in the hardware environment, a set of preliminary conducted experiments was used.

The hardware-in-loop (HIL) setup was used, which emulated an electric sport utility vehicle with four independent in-wheel motor powertrains in dynamically changing and vaguely defined environmental conditions. The core of the setup was represented by a decoupled testbed created by the ZF TRW Automotive® (Koblenz, Germany), connected to the high-precision vehicle dynamic software IPG CarMaker® (Karlsruhe, Germany). This testbed ensures smooth coordination between FB and RB, fast response time, flexible packaging, and integration with other chassis and powertrain control systems. To reproduce real pressure dynamics, the brake line pressure is measured there in the four brake calipers in a range of 20 MPa with a frequency of 1 kHz. The HIL system under investigation provided separate control of each of the four wheels using two interacted electrical drives. The electrohydraulic brake of the HIL setup was connected to the host computer via the dSPACE® (Paderborn, Germany) modular platform with the hardware components responsible for analogue-to-digital and digital-to-analogue data converting in real-time experiments, the control of the testbed, and the communication with the EV simulator. The mainboard of the HIL platform distributed the tasks between four core processors and communicated with a local host computer featuring 32 channels at 16-bit resolution and conversion time of less than 5 μ s. The mass of the sport utility vehicle simulated by IPG CarMaker® was 2117 kg, and wheel radius was 0.2 m. It was assumed that the vehicle moves in a straight-line maneuver at a velocity of 100 km/h, fed by an electrical drive with a maximal permissible torque of 200 Nm, wheel speed of 157 rad/s, and inertia of 2.1 kgm^2 , connected to the wheel imitator through the gear with a ratio of 10.5.

Details of experimentation and the set of experimental braking curves for front and rear wheels were reported in [8]. The most remarkable of them rely on the front wheels, where both the EB and the FB are operated together, whereas for the rear wheels, the FB is not actuated. These plots are selected, combined, and mutually scaled in Figure 9. The curve (w FL, light blue) demonstrates the velocity of the front left wheel, which follows the vehicle longitudinal velocity (v , blue line). Its wheel slip (L%, purple), friction torque (TF , green), and electrical torque (TE , red) curves are displayed. On the dry asphalt, since the EB torque is not sufficient to retain the optimal slip, the control system requests the additional FB torque. At the end of the slowing down, the regeneration is turned off, and the FB completes the deceleration alone. On the icy road, regeneration lasts all the way, while the FB does not participate in braking, except for the end of the process. An evident chattering phenomenon at low velocity is seen in the experimental torque plots.

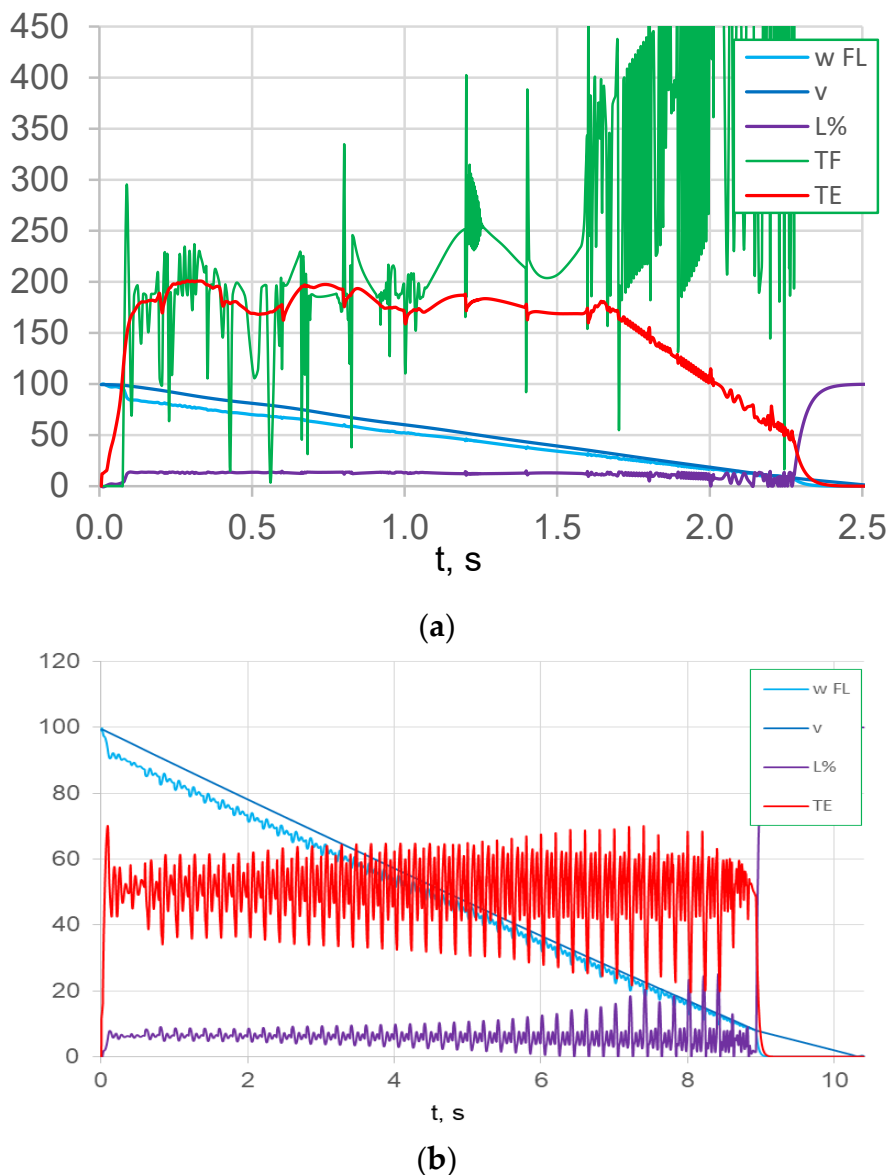


Figure 9. The traces obtained from the Hill setup (a) on dry asphalt and (b) on icy surface.

3.4. Simulation Results of the MRC Testing

Figure 10 introduces the traces obtained from the model shown in Figure 1. Here, in response to the electrical (TE) and friction (TF) torque, the application torque was allowed between the electrical (TE^*) and friction (TF^*) fractions, the first of which was limited to the value of 200 Nm. Since the EB response is fast and accurate, the application TE value turned out to be almost the same as the actuating TE^* , unless it exceeds the limitation of the value of 200 Nm. Since the EB response is fast and accurate, the application TE turned out to be almost the same as the actuating TE^* , unless it exceeds the limitation of the maximally electrical power. The torque oscillations are rather small here, as they are damped by the torque loop of the electrical drive. At low velocity, the friction increases dramatically, and the EB turns off.

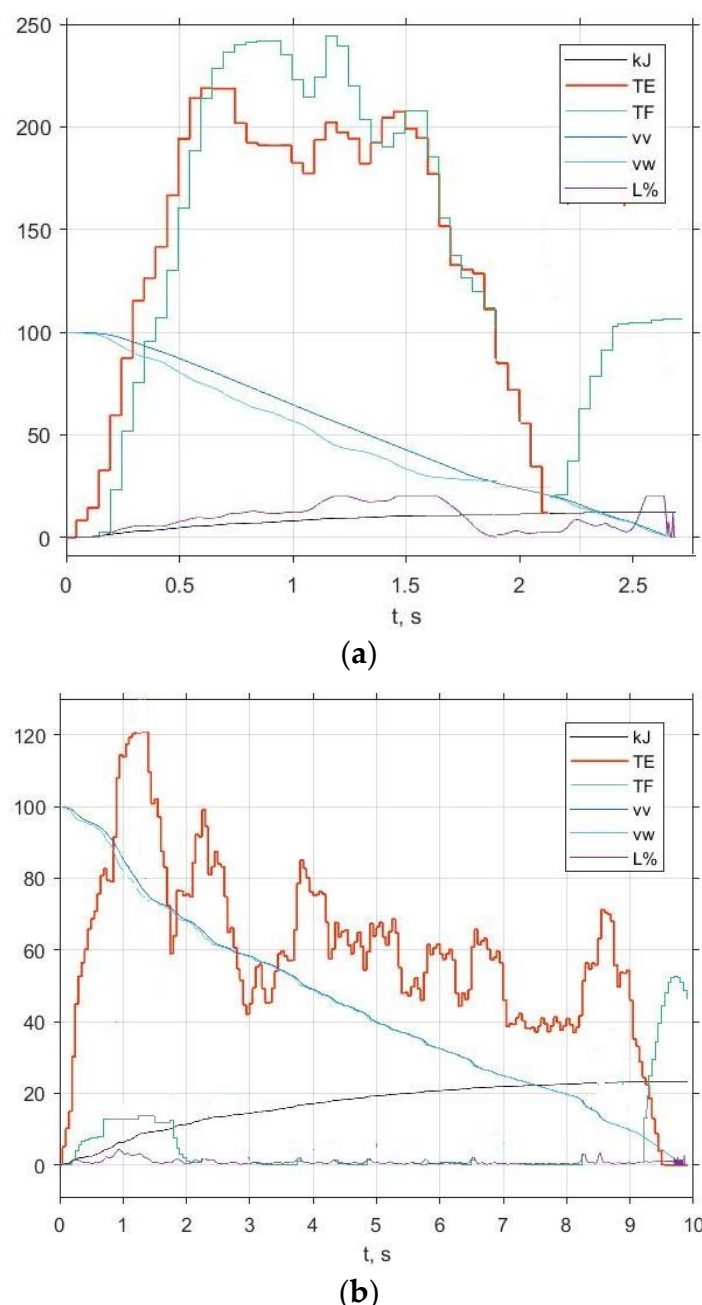


Figure 10. Simulation results: (a) dry asphalt and (b) icy surface.

3.5. Discussing the Concomitant Results

3.5. Discussing the Concomitant Results

In order to investigate the effect of the NN control, taking into account the assessment of the road surface, the motion of a vehicle on a changing pavement, from dry to icy conditions. Here, the system successfully detects a change of the road surface based on simulated. Figure 11 displays the traces obtained from the simulation of the volatile driving conditions. Here, the system successfully detects a change of the road surface on analysis of the torque gradient. At the beginning, the deceleration was around 30 m/s² on a dry surface. At the 1.5 s, the road surface suddenly changes from dry to icy. As the new gradient is recognized, the total application torque needed to ensure an intensive stop drops to 60 Nm. At the 1.5 s, the road surface suddenly changes from dry to icy, slow the car down within the optimal wheel slip zone. Therefore, only electrical braking is performed further. At low velocity, the EB turns off, and the FB runs alone. Herewith, an obvious reduction in chattering is observed in the torque plots at low velocity. First, this is because the designed model takes into account an increase of friction due to its static fraction. Second, because the torque loop of the electrical drive remains close

fraction. Second, because the torque loop of the electrical drive remains closed almost until the end.

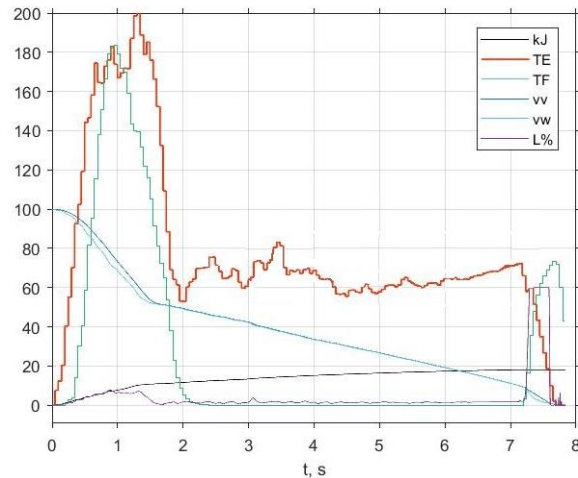


Figure 11. Simulation of the road changing from dry asphalt to icy surface.

Based on the energy curves (kJ, black) and assuming 50/50 regenerative efficiency, it turns that only 22 kJ of energy is delivered during braking on both roads (Figures 10 and 11). Now, it is useful to compare the MRC-driven system to the FLC-driven system published in [9]. This comparison displays MRC and NN stages of the FNN-driven system published in [10]. The NN-driven system plays also electrical torque of the EV. Approach braking, the MRC supports the same 60 Nm as experimental accurately. At gradual, the MRC, the MRC always keeps optimal wheel slip in all braking modes. Second, the NN-based system more accurately keeps the same braking times as the experimental system based on both the ABS mode (2 s) and gradual mode (10 s). Fourth, the torque chattering amplitude in the ABS mode (2.6 s) and gradual mode (10 s) is lower at worst, whereas the FLC-driven system has 280 Nm and the experimentally obtained oscillation exceeds 500 Nm at the end of braking. The NN control has 280 Nm and the experimentally obtained oscillation exceeds 500 Nm at the end of braking.

4. Conclusions

A comparison of the simulation and experimental results demonstrates that the created system demonstrates the desirable control behavior for various test scenarios, including both emergency and gradual braking.

A comparison of the simulation and experimental results demonstrates that the created system demonstrates the desirable control behavior for various test scenarios, including the proper system performance. The NN-driven system handles torque accurately. At both emergency and gradual braking, the EV velocity, slip, and torque responses confirm gradual braking, the MRC maintains the same 60 Nm as in the experiment and successfully firm the proper system performance. The NN-driven system handles torque accurately, keeps optimal wheel slip in both braking modes. The NN-based system demonstrates the same braking times as the experimental system, both in the ABS (2.6 s) and in gradual (10 s) modes. At the same time, the torque chattering upon the NN control is minimal. There, it stays within a 100 Nm band at worst, while the experimentally obtained oscillation exceeds 500 Nm at the end of braking.

By imitating changes in road conditions, the robustness of the designed MRC was evaluated. A comparison of the experimental and simulation results on two different pavements has proved good braking performance with the MRC. When trained on a combination of changing roads, the NN control model is able to make appropriate predictions for the surface on which the EV is traveling. The possibility of accurate execution indicates that the control system properly copes with the strong nonlinearity and cross coupling of the EV dynamics.

At the same time, the project also has the characteristics of flexible control and prospective coupling of the EV dynamics.

At the same time, the project also has the characteristics of flexible control and prospective applicability. This finding suggests that the NN structure deserves further investigation as a basis for intelligent control of automated EVs over their entire operating range. The NNC achieved better performance than the PIDC and FLC, given the complexity of the setup, the experience of the staff, and the time required to implement in the same

setup, the experience of the staff, and the time required to implement in the same control architecture. The assumed outcomes of this solution will be improved EV performance, increased mileage, and longer battery life.

Author Contributions: Conceptualization, methodology, software, writing, investigation, V.V.; validation, Z.R. and A.A.; resources, A.A.; project administration, funding acquisition, E.P. All authors have read and agreed to the published version of the manuscript.

Funding: This research was funded by the Estonian Research Council grant PRG 658.

Data Availability Statement: The data presented in this study are available on request from the corresponding author.

Conflicts of Interest: The authors declare no conflict of interest.

Abbreviations

ABS	antilock braking system
DOF	degree of freedom
EB	electrical brake
EV	electric vehicle
FB	friction brake
FLC	fuzzy logic controller
HES	hybrid energy storage
HIL	hardware-in-the-loop
kJ	recovered energy, kJ
λ , L%	p.u. and percentage wheel slip, appropriately
MRC	model reference controller
MSE	mean squared error, Nm
NN	neural network
NNC	neural network controller
NNEV	neural network model of an electric vehicle
PBEV	physics-based model of electric vehicle with blended braking
PIDC	proportional-integral-differential controller
REF	Reference
SOC	state of charge
TA	torque allocator
T^*, T	actuating and application braking torque, appropriately, Nm
TB^*	driver's reference, Nm
TE^*, TE	electrical fraction of actuating and application braking torque, appropriately, Nm
TF^*, TF	friction fraction of actuating and application braking torque, appropriately, Nm
v	longitudinal velocity of the vehicle, km/h
vw	longitudinal velocity of the wheel, km/h
w	angular speed of the wheel, rad/s

References

- Smil, V. Increasing energy inefficiency. *IEEE Spectrum*. 27 January 2021. Available online: <https://spectrum.ieee.org/energy-policy/increasing-energy-inefficiency> (accessed on 15 March 2021).
- Shang, M.; Chu, L.; Guo, J.; Fang, Y. Hydraulic braking force compensation control for hybrid electric vehicles. In Proceedings of the International Conference on Computer, Mechatronics, Control and Electronic Engineering (CMCE), Changchun, China, 24–26 August 2010; pp. 335–339.
- Savarese, S.M.; Tanelli, M. *Active Braking Control Systems Design for Vehicles*; Springer: London, UK, 2010; p. 200.
- Khastgir, S. The simulation of a novel regenerative braking strategy on front axle for an unaltered mechanical braking system of a conventional vehicle converted into a hybrid vehicle. In Proceedings of the 8th International Conference and Exhibition on Ecological Vehicles and Renewable Energies (EVER), Monte Carlo, Monaco, 27–30 March 2013; pp. 1–6.
- Reif, K. (Ed.) *Brakes, Brake Control and Driver Assistance Systems: Function, Regulation and Components*; Springer: Friedrichshafen, Germany, 2014.
- Raud, Z.; Vodovozov, V. Reserves for regenerative braking of battery electric vehicles. In Proceedings of the Electric Power Quality and Supply Reliability Conference (PQ), Rakvere, Estonia, 11–13 June 2014; pp. 1–6.

7. Vodovozov, V.; Lehtla, T. Design considerations for propulsion drives of electric vehicles. In Proceedings of the 14th International Symposium “Topical Problems in the Field of Electrical and Power Engineering”, Pärnu, Estonia, 13–18 January 2014; pp. 35–39.
8. Aksjonov, A.; Vodovozov, V.; Augsburg, K.; Petlenkov, E. Design of regenerative anti-lock braking system controller for 4-in-wheel-motor drive electric vehicle with road surface estimation. *Int. J. Automot. Technol.* **2018**, *19*, 727–742. [[CrossRef](#)]
9. Vodovozov, V.; Raud, Z. Modelling of energy recovery in electric vehicles for various braking scenarios on changing road surfaces. *Renew. Energy Power Qual. J.* **2020**, *18*, 178–183. [[CrossRef](#)]
10. Naseri, F.; Farjah, E.; Ghanbari, T. An efficient regenerative braking system based on battery / supercapacitor for electric, hybrid, and plug-in hybrid electric vehicles with BLDC motor. *IEEE Trans. Veh. Technol.* **2017**, *66*, 3724–3738. [[CrossRef](#)]
11. Cecotti, M.; Larminie, J.; Azzopardi, B. Estimation of slip ratio and road characteristics by adding perturbation to the input torque. In Proceedings of the IEEE International Conference on Vehicular Electronics and Safety (ICVES), Istanbul, Turkey, 24–27 July 2012; pp. 31–36.
12. Hea, H.; Wang, C.; Jiaa, H.; Cuic, X. An intelligent braking system composed single-pedal and multi-objective optimization neural network braking control strategies for electric vehicle. *Appl. Energy* **2020**, *259*, 114172. [[CrossRef](#)]
13. Hong, W.; Chakraborty, I.; Wang, H. Parametric optimization problem formulation for connected hybrid electric vehicles using neural network based equivalent model. In Proceedings of the 2nd IEEE Connected and Automated Vehicles Symposium (IEEE CAVS), Honolulu, HI, USA, 22–23 September 2019; pp. 1–6.
14. Zhang, X.; Lin, H. UAV anti-skid braking system simulation. In Proceedings of the 37th Chinese Control Conference, Wuhan, China, 25–27 July 2018; pp. 8453–8458.
15. Kadouaki, S.; Ohishi, K.; Hata, T.; Iida, N.; Takagi, M.; Sano, T.; Yasukawa, S. Antislip adhesion control based on speed sensorless vector control and disturbance observer for electric commuter train AT series 205-5000 of the east Japan railway company. *IEEE Trans. Ind. Electron.* **2007**, *54*, 2001–2008. [[CrossRef](#)]
16. Sanjay, K.M.; Lim, C.-C. A neural network based anti-skid brake system. *Discret. Contin. Dyn. Syst.* **1999**, *5*, 321–338. [[CrossRef](#)]
17. Wang, B.; Guan, H.; Lu, P.; Zhang, A. Road surface condition identification approach based on road characteristic value. *J. Terramech.* **2014**, *56*, 103–117. [[CrossRef](#)]
18. Bhandari, R.; Patil, S.; Singh, R.K. Surface prediction and control algorithms for anti-lock brake system. *Transp. Res.* **2012**, *21 Pt C*, 181–195. [[CrossRef](#)]
19. Ngwangwa, H.M.; Heyns, S.; Labuschagne, F.; Kululanga, G.K. Overview of the neural network based technique for monitoring of road condition via reconstructed road profiles. In Proceedings of the 27th Southern African Transport Conference (SATC), Pretoria, South Africa, 7–11 July 2008; pp. 312–329.
20. Shyrokau, B.; Wang, D.; Savitski, D.; Ivanov, V. Vehicle dynamics control with energy recuperation based on control allocation for independent wheel motors and brake system. *Int. J. Powertrains* **2013**, *2*, 153–181. [[CrossRef](#)]
21. Venture, G.; Ripert, P.-J.; Khalil, W.; Gautier, M.; Bodson, P. Modeling and identification of passenger car dynamics using robotics formalism. *IEEE Trans. Intell. Transp. Syst.* **2006**, *7*, 349–359. [[CrossRef](#)]
22. Šabanovič, E.; Žuraulis, V.; Prentkovskis, O.; Skrīkāj, V. Identification of road-surface type using deep neural networks for friction coefficient estimation. *Sensors* **2020**, *20*, 612. [[CrossRef](#)]
23. Topić, J.; Škugor, B.; Deur, J. Neural network-based modeling of electric vehicle energy demand and all electric range. *Energies* **2019**, *12*, 1396. [[CrossRef](#)]
24. Cerdeira-Corujo, M.; Costas, A.; Delgado, E.; Barreiro, A.; Banos, A. Gain-scheduled wheel slip reset control in automotive brake systems. In Proceedings of the International Symposium on Power Electronics, Electrical Drives, Automation and Motion (SPEEDAM), Anacapri, Italy, 22–24 June 2016; pp. 1255–1260.
25. Kiyakli, O.; Solmaz, H. Modeling of an electric vehicle with MATLAB/Simulink. *Int. J. Automot. Sci. Technol.* **2018**, *2*, 9–15. [[CrossRef](#)]
26. Mann, G.K.I.; Hu, B.-G.; Gosine, R.G. Analysis of direct action fuzzy PID controller structures. *IEEE Trans. Syst. Man Cybern. Part B Cybern.* **1999**, *29*, 371–388. [[CrossRef](#)] [[PubMed](#)]
27. An, X.; Zhu, W.; An, N. Control system optimization of spillage brake based on RBF neural network. *Concurr. Comput. Pract. Exp.* **2020**, *32*. [[CrossRef](#)]
28. Wu, Y.; Wang, C.; Zhou, L.; Ou, L. A simulation of vehicle lateral stability based on fuzzy PID control. In Proceedings of the International Conference on Measuring Technology and Mechatronics Automation, Zhangjiajie, China, 11–12 April 2009; pp. 194–199.
29. Fu, Q.; Zhao, L.; Cai, M.; Cheng, M.; Sun, X. Simulation research for quarter vehicle ABS on complex surface based on PID control. In Proceedings of the 2nd International Conference on Consumer Electronics, Communications and Networks (CECNet), Yichang, China, 21–23 April 2012; pp. 2072–2075.
30. Li, W.; Zhu, X.; Ju, J. Hierarchical braking torque control of in-wheel-motor-driven electric vehicles over CAN. *IEEE Access* **2018**, *6*, 65189–65198. [[CrossRef](#)]
31. Ahmad, F.; Hudha, K.; Mazlan, S.A.; Jamaluddin, H.; Aparow, V.R.; Yunus, M.R.M. Simulation and experimental investigation of vehicle braking system employing a fixed caliper based electronic wedge brake. *Simul. Trans. Soc. Mod. Simul. Int.* **2018**, *94*, 327–340. [[CrossRef](#)]
32. Algadah, K.M.; Alaboodi, A.S. Anti-lock braking system components modelling. *Int. J. Innov. Technol. Explor. Eng.* **2019**, *9*, 3969–3975. [[CrossRef](#)]

33. Tan, H.-S.; Chin, Y.-K. Vehicle antilock braking and traction control: A theoretical study. *Int. J. Syst. Sci.* **1992**, *23*, 351–365. [[CrossRef](#)]
34. Perić, S.L.; Antić, D.S.; Milovanović, M.B.; Mitić, D.B.; Milojković, M.T.; Nikolić, S.S. Quasi-sliding mode control with orthogonal endocrine neural network-based estimator applied in anti-lock braking system. *IEEE/ASME Trans. Mechatron.* **2016**, *21*, 754–764. [[CrossRef](#)]
35. Bamigboye, O.O.; Obaje, S.E. Intelligent automatic car braking control system using neural network classifier. *Int. J. Eng. Invent.* **2016**, *5*, 51–56.
36. Cabrera, J.A.; Ortiz, A.; Castillo, J.J.; Simón, A. A fuzzy logic control for antilock braking system integrated in the IMMa tire test bench. *IEEE Trans. Veh. Technol.* **2005**, *54*, 1937–1949. [[CrossRef](#)]
37. Muliadi, J.; Kusumoputro, B. Neural network control system of UAV altitude dynamics and its comparison with the PID control system. *Hindawi J. Adv. Transp.* **2018**. [[CrossRef](#)]
38. Kuutti, S.; Bowden, R.; Joshi, H.; de Temple, R.; Fallah, S. Safe deep neural network-driven autonomous vehicles using software safety cages. In Proceedings of the 20th International Conference on Intelligent Data Engineering and Automated Learning (IDEAL), Manchester, UK, 14–16 November 2019; pp. 1–11.
39. Mirzaeinejad, H. Robust predictive control of wheel slip in antilock braking systems based on radial basis function neural network. *Appl. Soft Comput.* **2018**, *70*, 318–329. [[CrossRef](#)]
40. Gurkaynak, Y.; Khaligh, A.; Emadi, A. Neural adaptive control strategy for hybrid electric vehicles with parallel powertrain. In Proceedings of the IEEE Vehicle Power and Propulsion Conference (VPPC), Lille, France, 1–3 September 2010; pp. 1–6. [[CrossRef](#)]
41. Chae, H.; Kang, C.M.; Kim, B.D.; Kim, J.; Chung, B.D.; Choi, J.W. Autonomous braking system via deep reinforcement learning. In Proceedings of the IEEE 20th International Conference on Intelligent Transportation Systems (ITSC), Yokohama, Japan, 16–19 October 2017; pp. 1–6.
42. Modia, S.; Bhattacharyaa, J.; Basak, P. Estimation of energy consumption of electric vehicles using deep convolutional neural network to reduce driver's range anxiety. *ISA Trans.* **2020**, *98*, 454–470. [[CrossRef](#)]
43. Kiddee, K. Hybrid energy harvesting system based on regenerative braking system and suspension energy harvesting for middle electric vehicle. *TNI J. Eng. Technol.* **2020**, *8*, 29–38.
44. Morsalin, S.; Mahmud, K.; Town, G. Electric vehicle charge scheduling using an artificial neural network. In Proceedings of the IEEE Innovative Smart Grid Technologies–Asia (ISGT-Asia), Melbourne, Australia, 28 November–2 December 2016; pp. 276–280. [[CrossRef](#)]
45. Min, K.; Yeon, K.; Jo, Y.; Sim, G.; Sunwoo, M.; Han, M. Vehicle deceleration prediction based on deep neural network at braking conditions. *Int. J. Automot. Technol.* **2020**, *21*, 91–102. [[CrossRef](#)]
46. Dagher, K.A.; Al-Araji, A.S. Design of an adaptive PID neural controller for continuous stirred tank reactor based on particle swarm optimization. *Al-Khwarizmi Eng. J.* **2013**, *9*, 46–53.
47. Al-Khayyt, S.Z.S. Tuning PID controller by neural network for robot manipulator trajectory tracking. *Al-Khwarizmi Eng. J.* **2013**, *8*, 19–28.
48. Nepomnyashchiy, O.; Kazakov, F.; Ostroverkhov, D.; Tarasov, A.; Sirotinina, N. A neural regulator for efficient control of electric vehicle motors. *EAI Endorsed Trans. Energy Web* **2020**, *7*, 1–8. [[CrossRef](#)]
49. Aamir, M. On replacing PID controller with ANN controller for DC motor position control. *Int. J. Res. Stud. Comput.* **2013**, *2*, 21–29. [[CrossRef](#)]
50. Marino, A.; Neri, F. PID Tuning with Neural Networks. In *International Information and Database Systems*; Springer: Cham, Switzerland, 2019; pp. 477–487.
51. Slama, S.; Errachdi, A.; Benrejeb, M. Neural adaptive PID and neural indirect adaptive control switch controller for nonlinear MIMO systems. *Hindawi Math. Probl. Eng.* **2019**, *1*–11. [[CrossRef](#)]
52. Gao, S.; Yang, J.; Wang, J. D-FNN based modeling and BP neural network decoupling control of PVC stripping process. *Hindawi Math. Probl. Eng.* **2014**, *1*–13. [[CrossRef](#)]
53. Ziqiang, C.; Lin, Y. Intelligent anti-lock braking control of hybrid buses. *J. Automot. Saf. Energy* **2010**, *1*, 40–48.
54. Lie, G.; Zejian, R.; Pingshu, G.; Jing, C. Advanced emergency braking controller design for pedestrian protection oriented automotive collision avoidance system. *Hindawi Sci. World J.* **2014**. [[CrossRef](#)]
55. Tao, Y.; Xie, X.; Zhao, H.; Xu, W.; Chen, H. A regenerative braking system for electric vehicle with four in-wheel motors based on fuzzy control. In Proceedings of the 36th Chinese Control Conference, Dalian, China, 26–28 July 2017; pp. 4288–4293.
56. Gavin, H.P. *The Levenberg-Marquardt Algorithm for Nonlinear Least Squares Curve-Fitting Problems*; Duke University: Durham, NC, USA, 2020; p. 19.